LANGMUIR

pubs.acs.org/Langmuir Article

Critical Pressure Asymmetry in the Enclosed Fluid Diode

Jack R. Panter, Yonas Gizaw, and Halim Kusumaatmaja*

Cite This: *Langmuir* 2020, 36, 7463−7473 Read Online

ACCESS | Metrics & More | Article Recommendations | Supporting Information

ABSTRACT: Joint physically and chemically patterned surfaces can provide efficient and passive manipulation of fluid flow. The ability of many of these surfaces to allow only unidirectional flow means they are often termed fluid diodes. Synthetic analogues of these are enabling technologies from sustainable water collection via fog harvesting to improved wound dressings. One key fluid diode geometry features a pore sandwiched between two absorbent substrates—an important design for applications that require liquid capture while preventing back-flow. However, the enclosed pore is particularly challenging to design as an effective fluid diode due to the need for both a low Laplace pressure for liquid entering the pore and a high Laplace pressure to liquid leaving. Here, we calculate the Laplace pressure for fluid traveling in both directions on a range of conical pore designs with a chemical gradient. We show that this chemical gradient is in general required to achieve the largest critical pressure differences between incoming and outgoing liquids. Finally, we discuss the optimization strategy to maximize this critical pressure asymmetry.

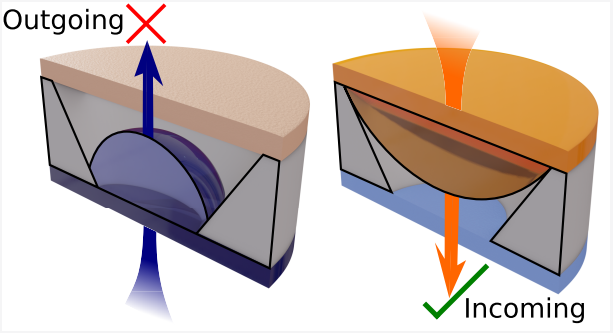

I. INTRODUCTION

Structured surfaces that control the direction of motion of liquid droplets are prevalent in nature.[1] Strong directionality is enabled by surfaces that have both physical and chemical gradients, demonstrated for example by the textured conical spines of the cactus *Opuntia microdasys*,[2] the spindle knots of spider silks,[3] and the ratcheted surface of butterfly wings.[4] This directionality is a result of a driving force from the combined effects of a Laplace pressure gradient across the droplet, caused by the physical structure,[5,6] and a surface energy gradient under the droplet, caused by a chemical pattern.[7,8]

Inspired by these biological examples, there is substantial interest in synthesizing structures that enforce unidirectional liquid flow − fluid diodes.[9] The technological applications of fluid diodes span numerous and ambitious fields focusing on efficiency and sustainability,[10] such as oil−water separation[11] and water purification or fog harvesting.[12] Fluid diodes are being realized in a range of geometries, such as across surface structures,[13] along a porous strip,[14] through the thickness of a material,[11] and within microfluidic channels.[15]

The optimal performance of a fluid diode relies on maintaining a high contrast in the force required to transport fluid through the diode in the forward direction compared to the reverse direction. One geometry in which this remains particularly challenging is the enclosed pore, illustrated in Figure 1. In this geometry, a pore through an impermeable membrane is sandwiched between two absorbent substrates. The diode ability here arises from the critical pressure asymmetry—the difference in the maximum Laplace pressure (critical pressure) required to force liquid from the bottom

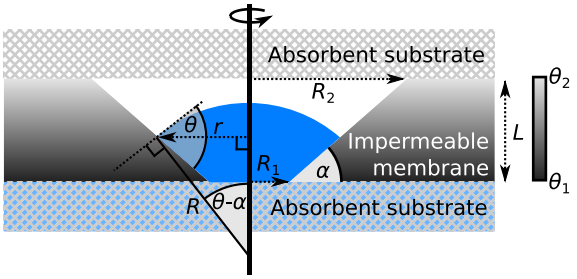

Figure 1. 2D illustration of the axisymmetric pore construction and outgoing meniscus profile. The axis of symmetry is shown as the thick vertical line. Liquid is shown in blue, with vapor shown in white.

substrate to the top substrate compared to the reverse direction. Such a design is particularly suited to a range of applications in which fluid should be readily absorbed into the diode but not be able to pass back out. Cleaning and hygiene are two notable areas where such applications are prominent. In these, the diode would both facilitate absorption of liquid from a surface, such as skin, into a porous material while also preventing back-flow out of the material. General and widely used potential applications include diapers, cloths, and

Received: April 13, 2020
Revised: June 2, 2020
Published: June 2, 2020

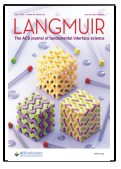

https://dx.doi.org/10.1021/acs.langmuir.0c01039
Langmuir 2020, 36, 7463−7473

towels.[16] However, the fluid diode is also gaining interest in high-performance innovations, such as sports textiles, which absorb and remove sweat to cool the body but are waterproof from the outside,[17] and wound dressings, in which excess fluid should be selectively absorbed out of the wound to improve healing and reduce infection risk.[18]

Here, we explore the diode capabilities of a conical pore augmented with a chemical gradient. Conical pores, or pores with a variation in cross-sectional width, have been shown in microfluidic fields to enable effective passive regulation of fluid flow, with a key application being the capillary burst valve.[15,19−21] Furthermore, substantial progress has been made in calculating the maximum Laplace pressures for liquid entering physically textured surfaces (see, for example, refs 22 and 23) as well as liquid exiting physically textured surfaces of axisymmetric and nonaxisymmetric cross sections.[24,25] However, the enclosed geometry, efficacy at preventing back-flow, and the impact of chemical patterning have never been discussed.

In section II.A, we begin by calculating the Laplace pressure for liquid leaving the pore. In section II.B, we calculate the Laplace pressure for liquid entering the pore. We then compare the incoming and outgoing maximum Laplace pressures using the critical pressure asymmetry to measure the strength of the diode in section III.C section before finally optimizing the chemical pattern to produce the maximum possible critical pressure asymmetry in section III.D.

II. THEORY

II.A. Outgoing Critical Pressures. The model setup, illustrated in Figure 1, features a liquid-impermeable membrane shown in shaded gray, punctured by an axisymmetric (conical) pore of wedge angle α. Without loss of generality, we restrict α to the interval $[0, \pi/2]$, so that the smallest pore radius R_1 is always located at the bottom of the system and the largest pore radius R_2 is located at the top. For $\alpha > \pi/2$, we need not perform additional calculations, but rather turn the pore as shown upside-down, and exchange the roles of incoming and outgoing critical pressure. In addition to a physical gradient, we employ a chemical gradient in the form of the local contact angle $\theta(r)$ which varies from θ_1 at the bottom of the pore to θ_2 at the top. Although any variation in contact angle can be chosen, we employ a linear variation to most closely compare with the linear physical gradient of the conic profile, where

$$\theta(r) = \theta_1 + (\theta_2 - \theta_1)\frac{r - R_1}{R_2 - R_1} \tag{1}$$

As the primary focus of this section is to model the pressure required for liquid to exit the pore, the contact angles used in the analysis throughout should be treated as the advancing contact angles on a surface where hysteresis is present.

In a fully enclosed pore, the top of the bottom surface of the liquid-impermeable membrane is in contact with liquid-absorbent substrates, shown as cross-hatched areas in Figure 1. For considering the outgoing critical pressure, the bottom absorbent substrate is modeled as an infinite liquid reservoir from which the liquid meniscus rises upward into the pore. The top substrate is modeled as a perfect liquid sink: as soon as liquid reaches the top of the pore or contacts the upper surface, the diode breaks down.

We consider the surface to be smooth with the only pinning sites occurring at the sharp corners at the top and bottom of the pore, and we work below the capillary length so that the liquid meniscus assumes a spherical cap geometry for all values of the contact line radius r. To ensure this, the pore size should typically be less than several millimeters; for example, the capillary length of water is 2.7 mm, while for a low surface tension liquid such as hexane the capillary length is 1.7 mm. We also consider the system to be larger than the longest range van der Waals forces (~100 nm[26]), so that disjoining-pressure modifications to the liquid−vapor interface shape close to the contact line are negligible. The pressure difference ΔP across the liquid−vapor interface is therefore described by the Young−Laplace equation appropriate for a spherical geometry: $\Delta P = 2\gamma_{lv}/R$, where γ_{lv} is the liquid−vapor interfacial tension and R is the radius of the sphere. This spherical cap model also implies we treat the fluid configurations as static; the impact of fluid velocity on burst pressures can also be important but is outside the scope of the current work. For instance, such dynamical effects have been studied in a variety of porous structures.[25,27,28] Throughout, we nondimensionalize the Laplace pressure so that $\Delta P_r = \Delta P/(2\gamma_{lv}/R_1)$. For convenience, we also nondimensionalize all radii with respect to R_1, so that for example $R' = R/R_1$ and $R_2' = R_2/R_1$.

We note here that although we label the fluids as "liquid" and "vapor", as the methods only require a knowledge of the contact angle at the three-phase contact line and the fluid−fluid interfacial tension, the analyses presented here are entirely general for any pair of immiscible fluids, such as oil and water.

By use of the construction in Figure 1, the outgoing Laplace pressure ΔP_r^{out} may be described as a function of the reduced contact line radius $r' = r/R_1$

$$\Delta P_r^{out} = \frac{1}{r'}\sin\left[\theta_1 + (\theta_2 - \theta_1)\frac{r' - 1}{R_2' - 1} - \alpha\right] \tag{2}$$

Finding the critical outgoing pressure ΔP_c^{out} then becomes finding the maximum value of ΔP_r as r' is increased from 1 to R_2'. As soon as the contact radius reaches R_2', the liquid will be spontaneously absorbed into the top substrate. It is possible that the apex of the meniscus contacts the upper substrate before $r' = R_2'$, but we reserve discussion of these cases to section II.A.5. To begin with, if we only allow liquid to be absorbed into the top substrate at $r' = R_2'$, and then ΔP_r^{out} exhibits four characteristic variations with r', depending on R_2', θ_1, θ_2, and α; representative examples of each are plotted in Figure 2a, where we fix $\alpha = 45°$ and $R_2' = 6$.

II.A.1. Variation 1 and the Bottom-Pinned (B) Critical Meniscus. The first variation, shown as the dotted red line, shows that for $r' > 1$ ΔP_r^{out} decreases monotonically with r'. When $r' = 1$, however, the contact line is pinned to the bottom of the pore. The Gibbs pinning criterion of a contact line at a sharp corner[29,30] then permits a continuum of allowed pressures, as the pinned contact angle may vary from θ_1 with respect to the bottom surface of the impenetrable membrane to θ_1 with respect to the sloping pore wall. This is shown as the vertical dotted red line at $r' = 1$. The critical pressure here occurs in the bottom-pinned state, labeled the B state in Figure 2b, where

$$\Delta P_c^{out}(B) = \sin\left[\min\left(\theta_1 - \alpha, \frac{\pi}{2}\right)\right] \tag{3}$$

https://dx.doi.org/10.1021/acs.langmuir.0c01039
Langmuir 2020, 36, 7463−7473

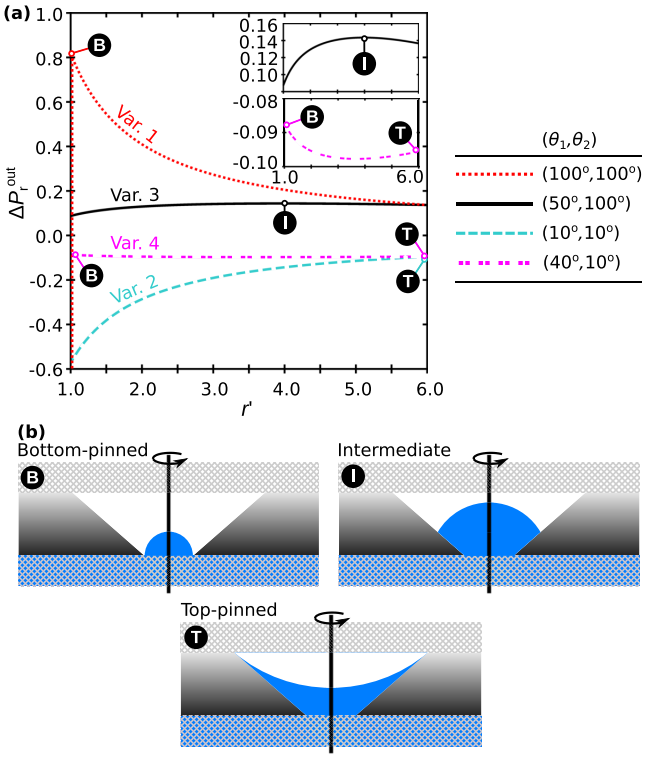

Figure 2. (a) Example plots of each of the four outgoing reduced pressure variations with r', with insets magnifying the local maxima/minima. The local maxima of each variation are associated with one of three critical meniscus types, illustrated in (b).

For $\theta_1 - \alpha < \pi/2$, $\Delta P_c^{out}(B)$ occurs when the interface depins from the sharp corner, such that the contact angle at the contact line is equal to θ_1. For $\theta_1 - \alpha > \pi/2$, however, $\Delta P_c^{out}(B)$ happens when the contact angle reaches $\pi/2 - \alpha$, before the depinning event, because the maximum possible critical pressure for the system is attained here at $R = R_1$.

II.A.2. Variation 2 and the Top-Pinned (T) Critical Meniscus. The second variation, shown as the dashed cyan line in Figure 2a, shows a monotonic increase of ΔP_r^{out} with r'. The critical pressure therefore occurs at the point when the contact line reaches the top of the system at $r' = R_2'$, where $\theta = \theta_2$. This is labeled the top-pinned (T) state in Figure 2b. In this case

$$\Delta P_c^{out}(T) = \frac{1}{R_2'}\sin(\theta_2 - \alpha) \tag{4}$$

II.A.3. Variation 3 and the Intermediate (I) Critical Meniscus. The third variation, shown as the solid black line in Figure 2a, exhibits a nonmonotonic variation with r' and a local maximum at intermediate values of r', labeled the I state in Figure 2b. The upper inset panel highlights the local maximum in a vertical magnification. To solve for the critical pressure, we aim to find stationary points of ΔP_r^{out} in eq 2, such that the critical contact line radius $r_c' \in (1, R_2')$. This amounts to solving

$$\frac{1}{r_c'}\left(\frac{\theta_2 - \theta_1}{R_2' - 1}\right)\cos\left(\theta_1 + (\theta_2 - \theta_1)\frac{r_c' - 1}{R_2' - 1} - \alpha\right) - \frac{1}{r_c'^2}\sin\left(\theta_1 + (\theta_2 - \theta_1)\frac{r_c' - 1}{R_2' - 1} - \alpha\right) = 0 \tag{5}$$

for r_c', such that ΔP_r^{out} is maximal, yielding $\Delta P_c^{out}(I)$. In general, this is not analytically solvable and instead must be solved numerically. Interestingly, such a local maximum cannot exist for a chemically homogeneous pore: rather, it is a result of the competition between physical and chemical gradients. To illustrate this, we consider the example shown in Figure 2a (solid black line), for which $\theta_1 < \pi/2$, but $\theta_2 > \pi/2$. Physically, as the contact line radius r' increases from 1 to R_2'; this tends to increase the droplet radius R' and hence reduce the magnitude of the Laplace pressure. Chemically, the simultaneous increase in local contact angle tends to reduce the droplet radius R and so increase the droplet pressure. When the I-state exists, it is therefore due to the balancing of these two effects.

II.A.4. Variation 4 and the B and T Critical Menisci. Instead of a local maximum, the fourth variation, shown as the double-dashed magenta line in Figure 2a, exhibits a local minimum. The lower inset panel highlights the local minimum in a vertical magnification. This behavior is observed when solving eq 5, which yields a minimal solution of ΔP_r^{out}. Thus, both the B state at $r' = 1$ and the T state at $r' = R_2'$ become local maximizers of ΔP_r^{out}. Which state globally maximizes ΔP_r^{out} is found by comparing eqs 3 and 4. We detail this comparison in section III.A.2. We further note here that both the B state and T state have negative Laplace pressures. It is possible for the B state to have negative Laplace pressure (whereby $\theta_1 < \alpha$) if θ_2 is so small that the Laplace pressure becomes more negative on increasing r' from 1 to R_2'.

II.A.5. Influence of Top Substrate: B′ and I′ Critical Menisci. When the liquid meniscus is convex, the center of the meniscus may contact the top of the pore before the B state or I state critical pressure is reached. We denote the bottom-pinned contacting state B′ and the intermediate contacting state I′. We note that a top-pinned contacting state cannot occur, as this would require the center of the meniscus to contact the top absorbent substrate before the three-phase contact line. For clarity of notation throughout, we refer to a liquid meniscus as being convex if the droplet forms a converging lens, such as the B state in Figure 2b, and concave if the droplet forms a diverging lens, such as the T state in Figure 2b. In Figure 3a, we construct the total height of the liquid meniscus as the sum of the height of the contact line z_c above

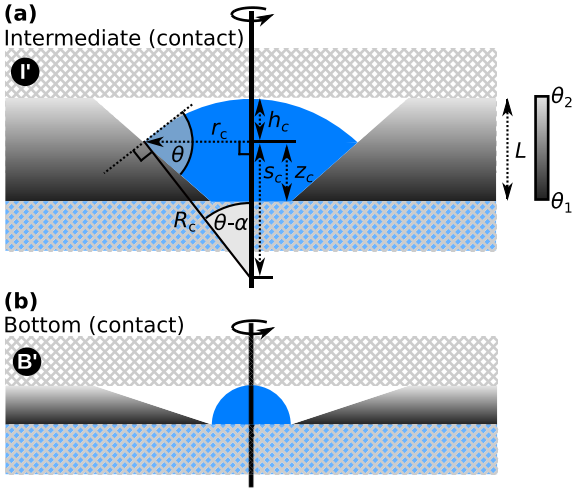

Figure 3. (a) Construction used to calculate the critical pressure of the I′ state. (b) Illustration of the B′ state, with the point of failure highlighted by a red circle.

https://dx.doi.org/10.1021/acs.langmuir.0c01039
Langmuir 2020, 36, 7463−7473

the pore bottom and the height of the spherical cap above this h_c. Noticing that $h_c = R_c - s_c$, where s_c is the z-distance from the center of the spherical cap to the contact line, we derive

$$h_c = r_c \frac{1 - \cos(\theta(r_c) - \alpha)}{\sin(\theta(r_c) - \alpha)} \tag{6}$$

For the spherical cap to touch the upper substrate, $z_c + h_c = L$ must be satisfied, where $z_c = (r_c - R_1)\tan\alpha$ and the membrane thickness $L = (R_2 - R_1)\tan\alpha$. In reduced units, this amounts to solving

$$(r_c' - R_2')\tan\alpha + r_c' \frac{1 - \cos(\theta(r_c') - \alpha)}{\sin(\theta(r_c') - \alpha)} = 0 \tag{7}$$

In general, this does not have analytic solutions and must be solved numerically. Once r_c' is found in this way, it is straightforward to substitute r' for r_c' in eq 2 to recover the critical pressure $\Delta P_c^{out}(I')$ caused by the cap contacting the upper substrate, while the contact line radius takes an intermediate value between R_1 and R_2.

If instead the contact line is pinned to the bottom of the pore at the point of meniscus contact, as illustrated in Figure 3b, the B′-type critical meniscus arises, where the outgoing critical pressure may be simply expressed as

$$\Delta P_c^{out}(B') = \frac{2}{L' + \frac{1}{L'}} \tag{8}$$

where $L' = L/R_1$.

II.B. Incoming Critical Pressures. We model the occurrence of liquid entering the pore from above in Figure 4. We utilize the same setup as shown in Figure 1, with the

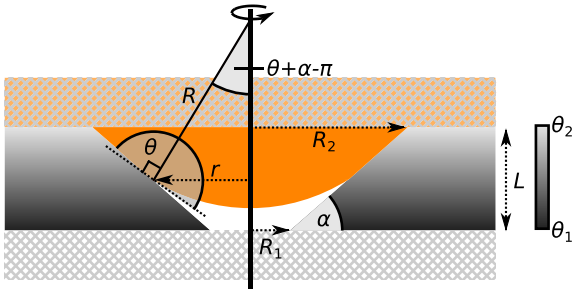

Figure 4. 2D illustration of the axisymmetric pore construction and incoming meniscus profile. The axis of symmetry is shown as the thick vertical line. Liquid is shown in orange, with air shown in white.

exception that the liquid (orange) now enters from the top absorbent substrate and the bottom substrate is dry. The same linear physical and chemical gradients are employed as before. Again, as we focus on modeling the maximum pressure maintainable before fluid enters the pore, the contact angles used in the analysis are the advancing contact angles on a surface where hysteresis is present.

The incoming Laplace pressure ΔP_r^{in} can be derived as

$$\Delta P_r^{in} = -\frac{1}{r'} \sin\left[\theta_1 + (\theta_2 - \theta_1)\frac{r' - 1}{R_2' - 1} + \alpha\right] \tag{9}$$

It can be seen that eq 9 can be obtained from ΔP_r^{out} in eq 2 by exchanging the fluid phases, such that $\theta(r') \to \pi - \theta(r')$. This simple transformation, however, will be shown to give rise to remarkably different incoming and outgoing critical pressures.

Again, the competition between physical and chemical gradients gives rise to four different variations in ΔP_r^{in} with r', where we have reserved the study of the interaction between the meniscus apex and lower absorbent substrate to section II.B.5. The characteristic examples of each shown in Figure 5a illustrate the symmetry between ΔP_r^{in} and ΔP_r^{out}, as it is observed that by making the fluid exchange, Figure 2a is reflected in the r'-axis to yield Figure 5a.

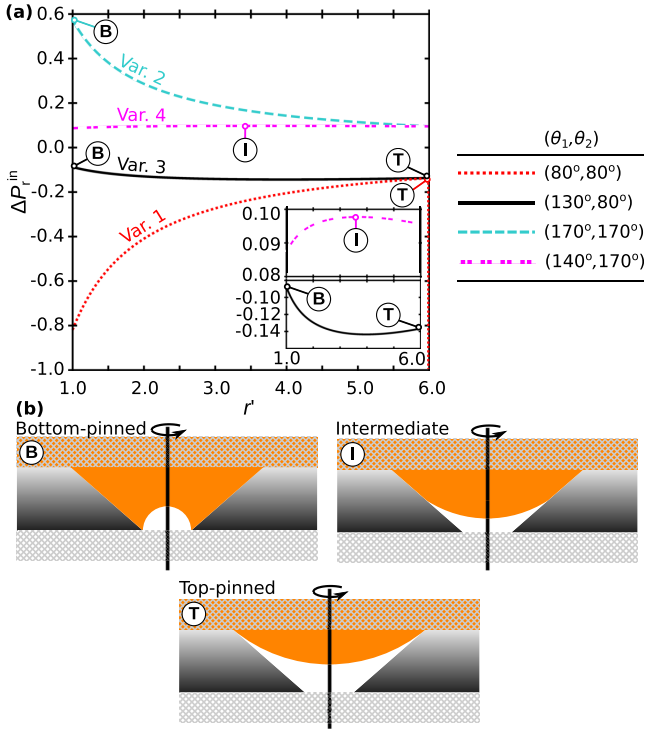

Figure 5. (a) Example plots of each of the four incoming reduced pressure variations with r', with insets magnifying the local maxima/minima. The local maxima of each variation are associated with one of three critical meniscus types, illustrated in (b).

II.B.1. Variation 1 and the Top-Pinned (T) Critical Meniscus. The first variation is shown as the dotted red line in Figure 5a. Here, for $r' < R_2'$, ΔP_r^{in} decreases monotonically as r' decreases. When $r' = R_2'$, however, a range of critical pressures is possible as the contact line is pinned to the top of the pore. This is shown as the vertical dotted red line at $r' = R_2'$. The critical pressure here occurs in the top-pinned state, labeled the T-state in Figure 5b, where

$$\Delta P_c^{in}(T) = -\frac{1}{R_2'} \sin(\theta_2 + \alpha) \tag{10}$$

II.B.2. Variation 2 and the Bottom-Pinned (B) Critical Meniscus. The second variation is shown as the dashed cyan line in Figure 5a. This shows a monotonic increase of ΔP_r^{in} as r' is decreased. The critical pressure therefore occurs at the point when the contact line reaches the bottom of the system at $r' = 1$ and $\theta = \theta_1$, labeled the B state in Figure 5b. In this case

$$\Delta P_c^{in}(B) = -\sin(\theta_1 + \alpha) \tag{11}$$

II.B.3. Variation 3 and the T and B Critical Menisci. The third variation is shown as the solid black line in Figure 5a. Here, a local minimum exists at intermediate values of r'. The lower inset panel highlights the local minimum in a vertical

https://dx.doi.org/10.1021/acs.langmuir.0c01039
Langmuir 2020, 36, 7463−7473

magnification. In this pressure variation, both the T state and B state become local maximizers of ΔP_r^{in}. Which state globally maximizes ΔP_r^{in} is found by comparing eqs 10 and 11. We perform this comparison for selected examples of θ_1 and θ_2 in section III.B.2.

II.B.4. Variation 4 and the Intermediate (I) Critical Meniscus. The fourth variation is shown as the double-dashed magenta line in Figure 5a. Here, a local maximum is observed at intermediate values of r', labeled the I state in Figure 5b. The upper inset panel in Figure 5a highlights the local maximum in a vertical magnification. This local maximum can be found by finding stationary points of ΔP_r^{in} in eq 9 which maximize ΔP_r^{in} in the interval $r_c' \in [1, R_2']$. This is achieved through solving

$$\frac{1}{r_c'}\left(\frac{\theta_2-\theta_1}{R_2'-1}\right)\cos\left(\theta_1+(\theta_2-\theta_1)\frac{r_c'-1}{R_2'-1}+\alpha\right) - \frac{1}{r_c'^2}\sin\left(\theta_1+(\theta_2-\theta_1)\frac{r_c'-1}{R_2'-1}+\alpha\right)=0 \quad (12)$$

In general, this is again not analytically solvable and instead must be solved numerically.

II.B.5. Influence of Top Substrate: T′ and I′. When the liquid meniscus is convex, the center of meniscus may contact the bottom of the pore before the T state or I state critical pressure is reached.

To find the critical pressure of the I-contacting state shown in Figure 6a (denoted I′), we begin by finding the total sag

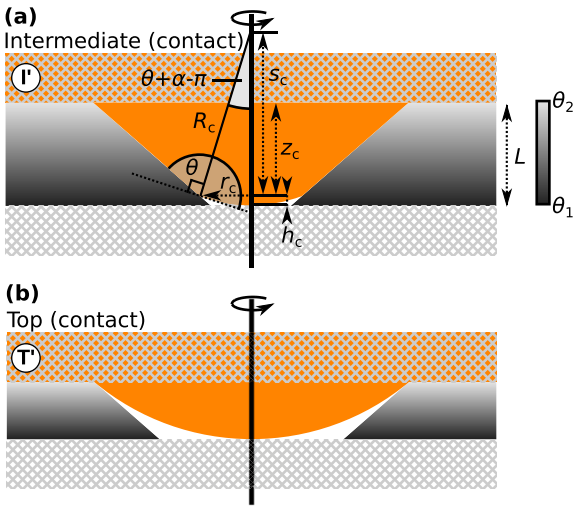

Figure 6. (a) Construction used to calculate the critical pressure of the I′ state. (b) Illustration of the B' state, with the point of failure highlighted by a red circle.

depth of the liquid meniscus. This is constructed as the sum of the depth of the contact line z_c below the pore top and the depth of the spherical cap below this h_c. Using $h_c = R_c - s_c$, we derive

$$h_c = -r_c\frac{1+\cos(\theta(r_c)+\alpha)}{\sin(\theta(r_c)+\alpha)} \quad (13)$$

The spherical cap will touch the lower substrate if $z_c + h_c = L$. In reduced units, we therefore solve

$$(1-r_c')\tan\alpha - r_c'\frac{1+\cos(\theta(r_c')+\alpha)}{\sin(\theta(r_c')+\alpha)} = 0 \quad (14)$$

In general, this does not have analytic solutions and must be solved numerically. Once r_c' is found in this way, we substitute r' for r_c' in eq 9 to obtain the critical pressure $\Delta P_c^{in}(I')$ caused by the cap contacting the lower substrate, while the contact line radius takes an intermediate value between R_1 and R_2.

If instead the contact line remains pinned to the top of the pore at the point of meniscus contact, as illustrated in Figure 6b, the top-contacting critical meniscus arises (denoted T′), where the incoming critical pressure is expressed as

$$\Delta P_c^{in}(T') = \frac{2}{L' + \frac{R_2'^2}{L'}} \quad (15)$$

III. RESULTS AND DISCUSSION

III.A. Outgoing Critical Pressures. *III.A.1. Critical Morphology Existence Ranges.* Overall, five different critical interface morphologies may occur: B, B′, T, I, and I′, in which the associated critical pressures feature different dependencies on θ_1, θ_2, α, and R_2'. Despite this complexity, the system parameters can be partitioned into four categories, determined based on whether the liquid meniscus is convex ($\theta > \alpha$) or concave ($\theta < \alpha$) at the top and bottom of the system. In Table 1, we show which critical morphology is possible within each category.

Table 1. Critical Outgoing Meniscus Types Able to Occur for a Convex Meniscus, $\theta > \alpha$, or Concave Meniscus, $\theta < \alpha$

	$\theta_1 > \alpha$	$\theta_1 < \alpha$
$\theta_2 > \alpha$	B, B′, I, I′	I, I′
$\theta_2 < \alpha$	B, B′	B, T

For $(\theta_1 > \alpha, \theta_2 < \alpha)$, the critical meniscus must occur when contact line is pinned to the bottom of the system in B or B′. For $(\theta_1 < \alpha, \theta_2 > \alpha)$, however, the Laplace pressure is negative when the contact line is at the bottom of the pore and positive at the top, so the critical meniscus must occur in some intermediate state: I or I′. For $(\theta_1 > \alpha, \theta_2 > \alpha)$, the meniscus is convex for all r, meaning the B, B′, I, or I′ states could occur. For $(\theta_1 < \alpha, \theta_2 < \alpha)$, the meniscus is concave for all r, so that the critical pressure must occur at either the bottom of the system, as B, or the top, as T.

III.A.2. Outgoing Critical Pressures Visualization. We now visualize how the outgoing critical pressure depends on the four parameters θ_1, θ_2, α, and R_2'. To reduce the dimensionality of the representation, in Figure 7 we show a matrix of contour plots at fixed θ_1 and θ_2, both of which may only take the values 10°, 50°, and 100°. We choose these values to capture the range of contact angles exhibited by commonly used liquids and substrates (see, for example, ref 31).

At each θ_1 and θ_2, Figure 7 illustrates the sets of critical pressure states presented in Table 1. We now discuss the competition between the states within each set for the global critical pressure.

When $\theta_1 = 10°$ and $\alpha < \theta_2$, B, B′, I, or I′ is possible; however, the I state is not observed within the range of R_2' plotted. The region of existence of B′ is shown to not depend on θ_2. This is because the B′ meniscus is pinned to the bottom of the well and so never experiences the chemical gradient.

https://dx.doi.org/10.1021/acs.langmuir.0c01039
Langmuir 2020, 36, 7463−7473

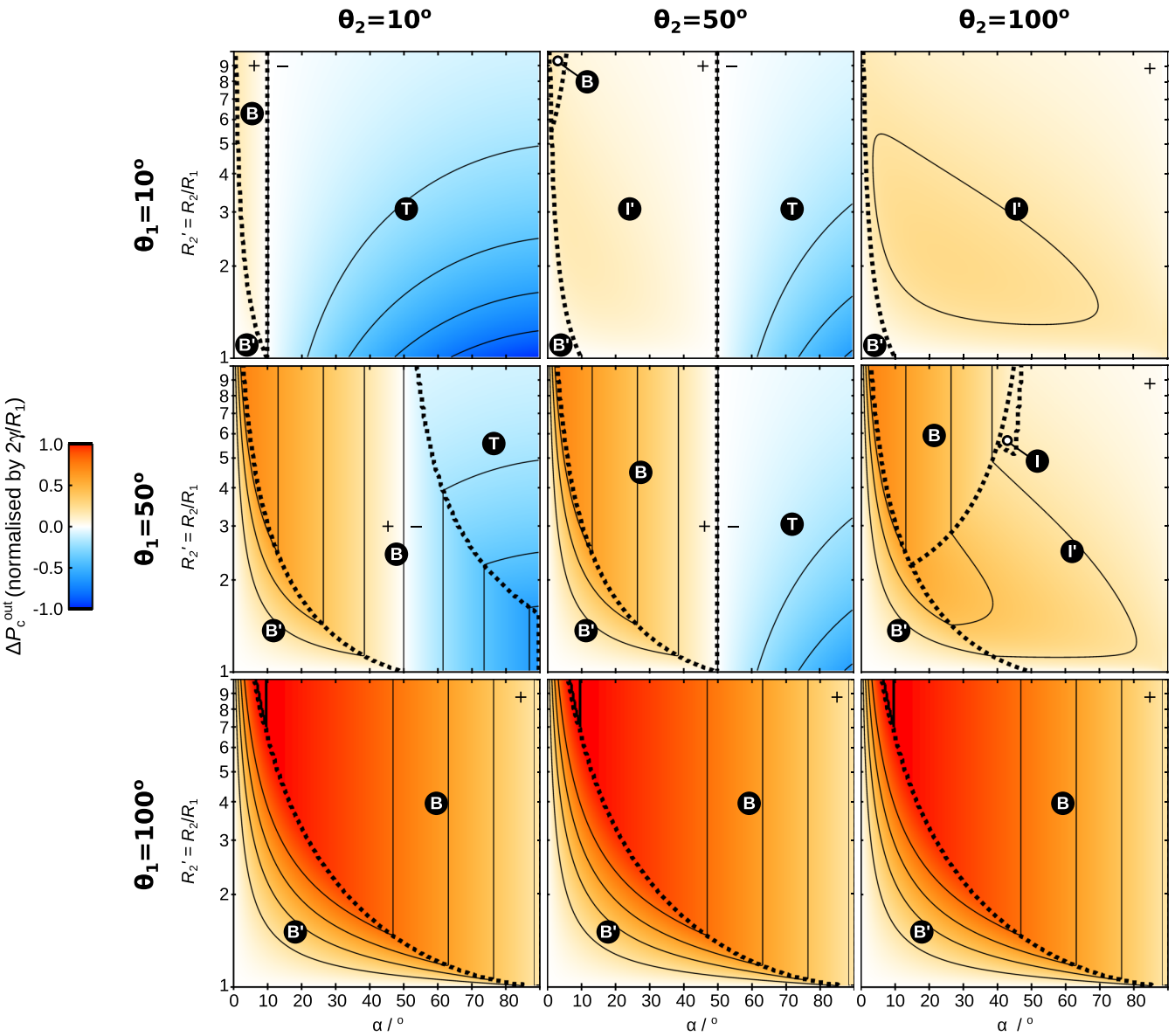

Figure 7. Matrix of R_2'–α contour plots of the outgoing critical pressure for a selection of θ_1 and θ_2. The outgoing meniscus types are labeled with black circles. The boundaries between these critical types are shown as dotted black lines. Contours are shown at intervals in ΔP_c^{out} of 0.2. For visual clarity, regions with $\Delta P_c^{out} > 0$ are marked with a "+" and regions where $\Delta P_c^{out} < 0$ are marked with a "−".

Furthermore, if B′ coexists with I′, the I′ state must necessarily have a lower critical pressure than B′. This is because, compared to B′, the I′ meniscus has a wider contact line radius and smaller peak height, leading to a greater radius of curvature and so a smaller critical pressure. Thus, the I′ critical pressure (which does depend on θ_2) never outcompetes the B′ critical pressure, leaving the B′ region of existence unaltered by θ_2. I′ is however able to outcompete the B state, as exhibited by the B region receding to larger R_2' values as θ_2 is increased from 10° to 50°.

When θ_1 = 50°, two additional features are observed. The first is that the B and T states only coexist and compete when $\theta_1 > \theta_2$ (and θ_1, $\theta_2 < \alpha$ as described in Table 1, meaning the menisci at the top and bottom of the pore are concave). This condition must be satisfied; otherwise, the wider aperture at the top of the pore will always produce a meniscus of larger negative critical radius, and so a greater critical pressure, than when pinned to the bottom of the pore. The second additional feature is that for θ_2 = 100° we now observe the I state to exist over a small region at large R_2'. For I to occur, the critical meniscus must be produced sufficiently low in the well for the peak to not contact the upper substrate. This requires a delicate balance between the chemical gradient (favoring the critical state at the top of the pore) and the physical gradient (favoring the critical state at the bottom of the pore), which overall produces a narrow existence range of I.

When θ_1 = 100°, only the B and B′ states can occur, as outlined in Table 1. Because the contact line at the critical pressure is always pinned to the bottom of the well, θ_2 has no impact on the critical pressure. Thus, all three contour plots for θ_1 = 100° are identical. Because $\theta_1 > 90°$, we also observe here the incidence of the maximum possible critical pressure, ΔP^{out} = 1, shown bounded by the thick contour. This is shown in eq 3 to be as a result of the B state critical pressure occurring when the contact line is pinned to the bottom of the well, with a contact angle of 90° with respect to the horizontal axis.

https://dx.doi.org/10.1021/acs.langmuir.0c01039
Langmuir 2020, 36, 7463−7473

III.B. Incoming Critical Pressures. *III.B.1. Critical Morphology Existence Ranges.* Overall, five different critical interface morphologies may occur: B, T, T′, I, and I′, in which the associated critical pressures feature different dependencies on θ_1, θ_2, α, and R_2'. Despite this, the critical pressure types able to occur within a system can be determined based on whether the liquid meniscus is convex ($\theta + \alpha > \pi$) or concave ($\theta + \alpha < \pi$) and the top and bottom of the system. This is presented in Table 2.

Table 2. Critical Incoming Meniscus Types Able to Occur for a Convex Meniscus, $\theta + \alpha > \pi$, or Concave Meniscus, $\theta + \alpha < \pi$

	$\theta_1 + \alpha > \pi$	$\theta_1 + \alpha < \pi$
$\theta_2 + \alpha > \pi$	T, T′, I, I′	T, T′
$\theta_2 + \alpha < \pi$	I, I′	T, B

For ($\theta_1 + \alpha < \pi$, $\theta_2 + \alpha > \pi$), the critical meniscus must occur when contact line is pinned to the top of the system as T or T′. For ($\theta_1 + \alpha > \pi$, $\theta_2 + \alpha < \pi$), however, the Laplace pressure is negative when the contact line is at the top of the pore and positive at the bottom, so the critical meniscus must occur in some intermediate state: I or I′. For ($\theta_1 + \alpha > \pi$, $\theta_2 + \alpha > \pi$), the meniscus is convex for all r, meaning the T, T′, I, or I′ states could occur. For ($\theta_1 + \alpha < \pi$, $\theta_2 + \alpha < \pi$), the meniscus is concave for all r, so that the critical pressure must either occur at the top of the system, as T, or the bottom, as B.

III.B.2. Incoming Critical Pressure Visualization. We now visualize how the incoming critical pressure depends on the four parameters θ_1, θ_2, α, and R_2'. To reduce the dimensionality of the representation, in Figure 8 we again show a matrix of contour plots at fixed θ_1 and θ_2, both of which may only take the values 10°, 50°, and 100°.

The incoming critical pressure contour plots in Figure 8 show markedly different behavior to the outgoing critical

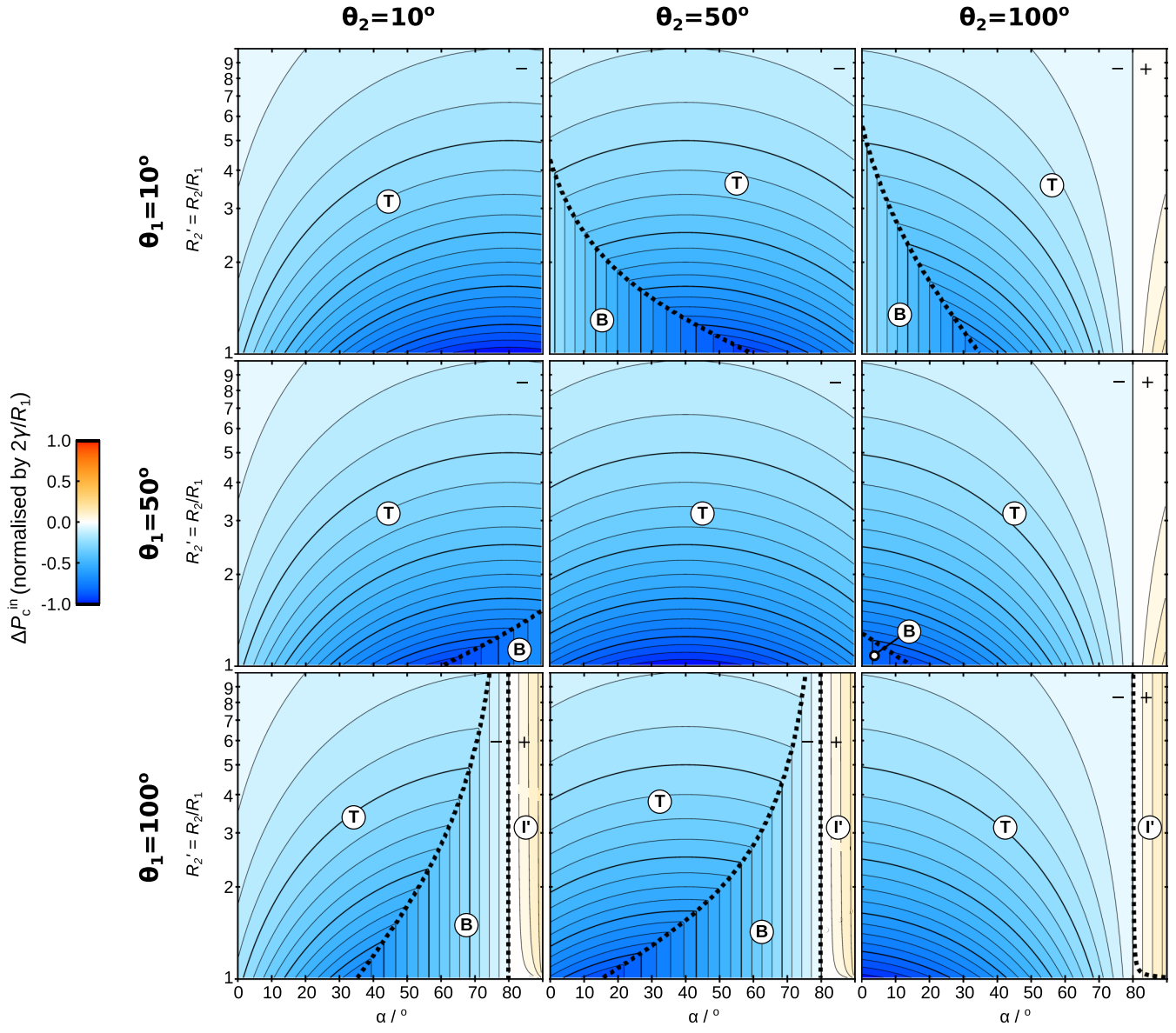

Figure 8. Matrix of R_2'–α contour plots of the incoming critical pressure for a selection of θ_1 and θ_2. The incoming meniscus types are labeled with white circles. The boundaries between these critical types are shown as dotted black lines. Contours are shown at intervals in ΔP_c^{in} of 0.05. For visual clarity, regions with $\Delta P_c^{in} > 0$ are marked with a "+" and regions where $\Delta P_c^{in} < 0$ are marked with a "−".

https://dx.doi.org/10.1021/acs.langmuir.0c01039
Langmuir 2020, 36, 7463−7473

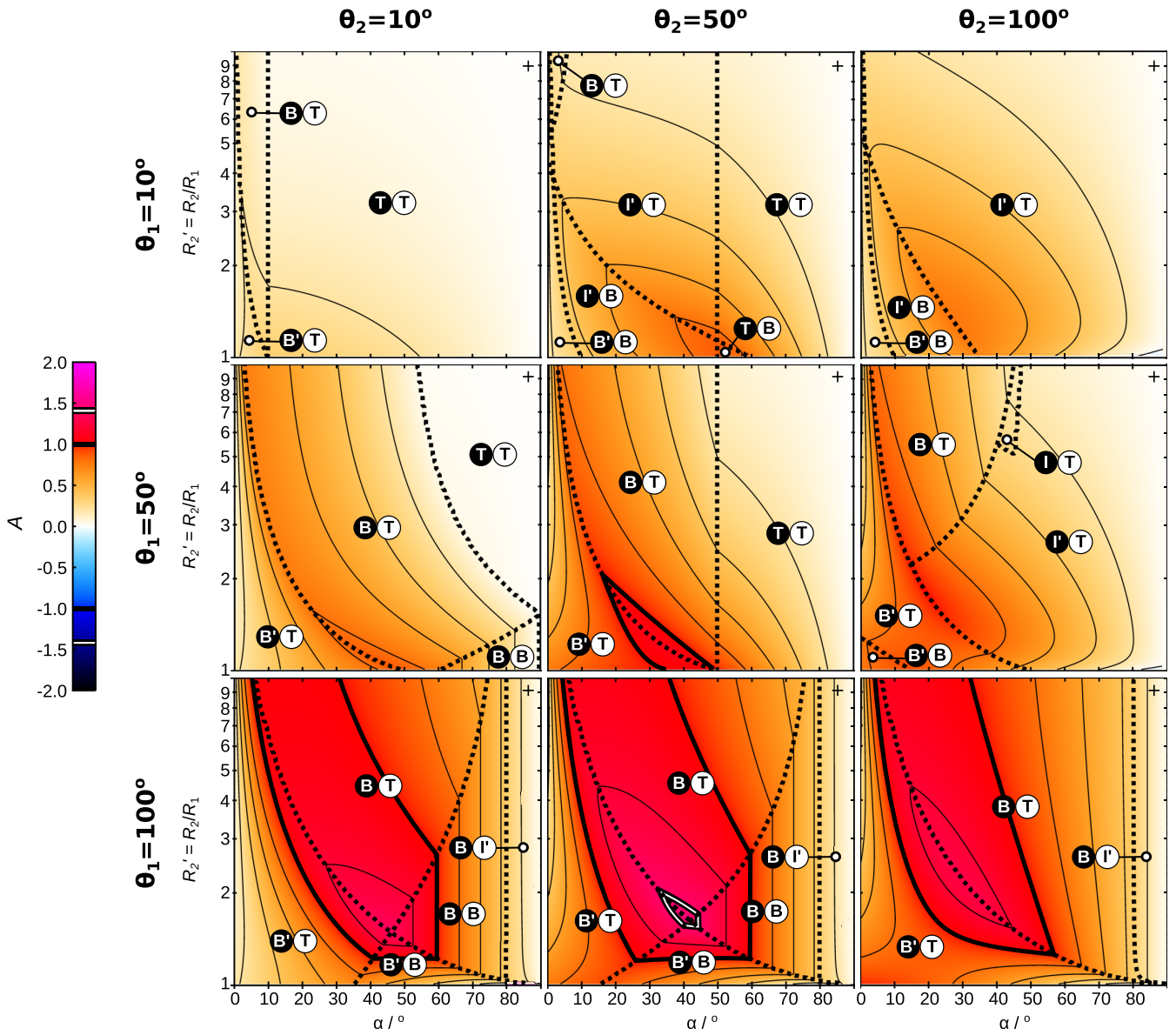

Figure 9. Matrix of $R_2'-\alpha$ contour plots of the critical pressure asymmetries for a selection of θ_1 and θ_2. The outgoing meniscus incoming meniscus pair types are labeled with black and white circles. The boundaries between these critical types are shown as dotted black lines. Contours are shown at intervals in A of 0.2. Two significant A contours are also highlighted: $A = 1$ (thick black line) and $A = \sqrt{2}$ (white-centered black line).

pressure plots in Figure 7. This is because under the range of θ_1 and θ_2 tested, except at large α, $\theta_1 + \alpha < \pi$ and $\theta_2 + \alpha < \pi$, meaning the liquid meniscus is concave. This means that the pore exerts a pulling force on the liquid in the top substrate, so that to prevent liquid filling the pore, a negative pressure must be applied.

Under such conditions, when $\theta_1 = \theta_2$, the T-type critical meniscus always emerges. This is because the meniscus has a wider contact radius at the top of the pore than the bottom, resulting in the less-negative critical pressure at the top of the pore. When $\theta_1 > \theta_2$, the B state may outcompete the T state for largest critical pressure at large α and R_2'. When this happens, the high contact angle at the bottom of the pore negates the small contact line radius to create a less-negative critical pressure than the T state. When $\theta_1 < \theta_2$, this time the B state may outcompete the T state for largest critical pressure at small α and R_2'. This is because at the bottom of the pore the low contact angle creates a liquid–vapor interface with a near-spherical shape. The associated large radius of curvature produces a smaller negative critical pressure than the meniscus at the top of the well.

When α is sufficiently large to enable $\theta_1 + \alpha > \pi$, the I′ state is observed. This is because a convex meniscus is enabled close to the bottom of the well, resulting in a positive critical pressure.

III.C. Critical Pressure Asymmetry. We now define the critical pressure asymmetry, A, of a pore: the difference between the outgoing and incoming critical pressures.

$$A = \Delta P_r^{\text{out}} - \Delta P_r^{\text{in}} \tag{16}$$

A matrix of contour plots shown in Figure 9 illustrates the rich and complex dependence of A on θ_1, θ_2, α, and R_2'. We identify three important values of A to consider, which are deduced in the Supporting Information (Figure S1). $A = \pm 1$, shown as the thick contour, is the maximum possible asymmetry for a doubly closed cylindrical pore when $R_2 \to \infty$. $A = \pm\sqrt{2}$,

https://dx.doi.org/10.1021/acs.langmuir.0c01039
Langmuir 2020, 36, 7463−7473

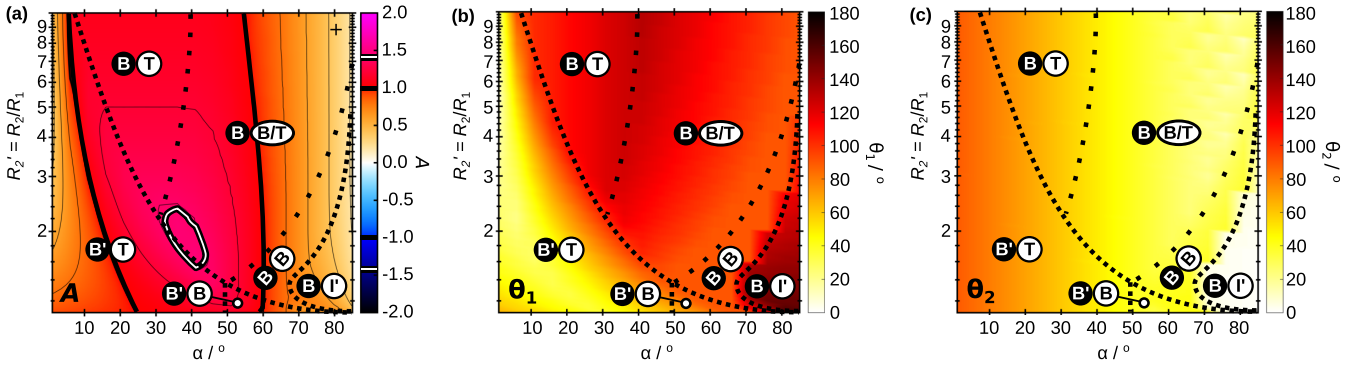

Figure 10. (a) Maximum asymmetry possible at each (α, R_2') coordinate. Two significant A limits are highlighted in the contour plots: $A = 1$ (thick black line) and $A = \sqrt{2}$ (white-centered black line). The outgoing meniscus incoming meniscus pair types are labeled with black and white circles, with dense dotted black lines showing the boundaries between these types. The diffuse black dotted line illustrates the approximate region where the incoming B and T states have equal pressure. (b) θ_1 required for maximum asymmetry. (c) θ_2 required for maximum asymmetry.

shown as the doubly thick contour, is the maximum possible asymmetry for a semiopen cylindrical pore. $A = 2$ is the maximum possible asymmetry for any pore. Recently, a semiopen pore has been developed which approaches this maximum.[25] We now discuss the features of the critical pressure asymmetries.

It is initially observed that for the range of parameters shown in Figure 9 A is never negative. This can be proved to be true in general for all $\alpha < \pi/2$, shown in Figure S2. Thus, for $\alpha < \pi/2$, a conical pore will always preferentially intake liquid than expel it.

For $\theta_1 = 10°$, the critical pressure asymmetry remains small. When $\theta_1 < \alpha$, A is small because both the incoming and outgoing critical pressures are negative (with the magnitude of the outgoing being smaller than the incoming). When $\theta_1 > \alpha$, A is also small as although the outgoing critical pressure is positive, it is never large. This is because $\Delta P_c^{out}(B)$ is small due to the low contact angle and $\Delta P_c^{out}(I')$ is small due to the large contact radius. Overall, the asymmetry is dominated by the negative contribution from the incoming critical pressure rather than the outgoing critical pressure. Because of the dominance of the incoming critical pressure, the maximal A occurs on the boundary between the incoming B and T critical meniscus types.

For $\theta_1 = 50°$, a similar picture emerges. However, now for $\theta_1 > \alpha$, the B- or B′-type outgoing critical pressure can be large and positive. In this region, we therefore begin to see larger A as the contribution of the outgoing critical pressure becomes more significant. The competition also becomes apparent between intermediate positive outgoing critical pressures (at small α, large R_2') and large negative incoming critical pressures (at intermediate α, small R_2'). The maximum asymmetries occur as an optimal compromise between these extremes, at intermediate α and R_2'. In contrast to $\theta_1 = 10°$, the maximum asymmetries now occur along an outgoing boundary.

For $\theta_1 = 100°$, very large asymmetries are observed, exceeding $A = 1$ in all panels examined and exceeding $A = \sqrt{2}$ when $\theta_2 = 50°$. Here, the large θ_1 enables large $\Delta P_c^{out}(B/B')$. Thus, the competition between large outgoing and incoming critical pressures observed for $\theta_1 = 50°$ becomes here more extreme. Interestingly, now that both the outgoing and incoming critical pressures can contribute equally to A, the maximum asymmetries are observed at points where an outgoing-type boundary and incoming-type boundary cross. This is most apparent when $\theta_1 = 100°$ and $\theta_2 = 50°$, where at the junction between the outgoing B/B′ boundary and incoming T/B boundary, $A > \sqrt{2}$.

III.D. Optimum Asymmetry. We observe in Figure 9 that the (α, R_2') coordinate that maximizes the asymmetry depends on both θ_1 and θ_2. We now investigate the maximum possible asymmetry for a specified α and R_2' by varying θ_1 and θ_2. This is achieved by evaluating the asymmetry at each (R_2', α) coordinate, when θ_1 and θ_2 are iteratively incremented in 2° steps from 0° to 180°. The overall optimum asymmetry is shown in Figure 10a, with the associated optimal θ_1 and θ_2 shown in Figures 10b and 10c, respectively.

Overall, we can conclude that the maximum possible asymmetry, $A = 1.46$, occurs at $\alpha = 41 \pm 5°$, $R_2' = 1.70 \pm 0.05$, $\theta_1 = 104 \pm 2°$, and $\theta_2 = 49 \pm 2°$. Uncertainties reported indicate the resolution with which the quantities were determined. Across all α and R_2', a key trend we observe is that a high contrast between θ_1 and θ_2 is required to produce maximum asymmetries (a homogeneous contact angle will not in general maximize A). We also observe that θ_1 and θ_2 vary nonmonotonically with both α and R_2' due to changes in the critical meniscus type.

We now examine the critical meniscus types observed to achieve maximum asymmetry. For the outgoing critical pressure, the observed strategy for maximizing A is to ensure the contact line remains pinned to the bottom of the pore in the B or B′ state, thereby ensuring ΔP_c^{out} remains large and positive.

The incoming critical meniscus type is, however, more variable, particularly in the region where the outgoing critical meniscus is the B state in the upper right-hand sides of the plots in Figure 10. Here, the incoming meniscus may be in the I′, T, or B states. In the region where I′ is dominant, the incoming critical pressure is positive, making this region unique across all α and R_2'. To maximize the asymmetry in this region, the most effective strategy is to maximize ΔP_c^{out} by using $\theta_1 \approx \alpha + \pi/2$ at the expense of enabling a positive incoming critical pressure. However, the large value of α ensures ΔP_c^{in} is never too large and is minimized further by setting $\theta_2 = 0°$.

When the I′ state does not occur, however, the B and T incoming states compete for the largest negative ΔP_c^{in}. As is observed in Figure 8, the largest negative critical pressures occur on the boundary between B and T (where this boundary exists). Thus, over the extended region outlined with diffuse

https://dx.doi.org/10.1021/acs.langmuir.0c01039
Langmuir 2020, 36, 7463−7473

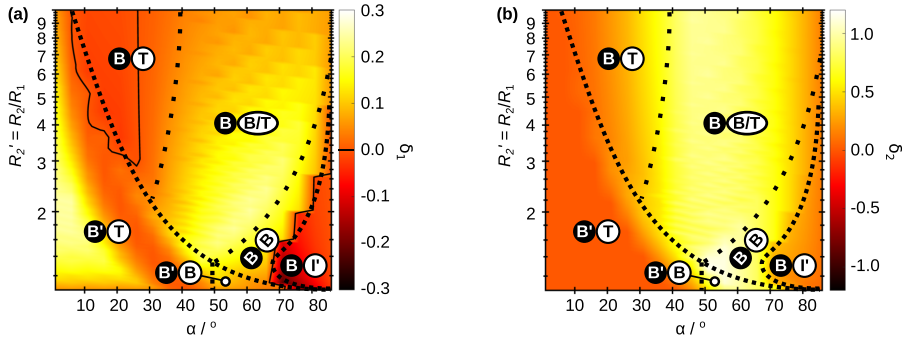

Figure 11. Comparison of the asymmetry of the optimal chemically patterned conical pore, with the sum of asymmetries from the same chemical patterning applied to a cylindrical pore, and a chemically homogeneous conical pore. The comparison is made for the chemically homogeneous conical pore with $\theta = \theta_1^{opt}$ in (a) and $\theta = \theta_2^{opt}$ in (b). Solid black contours mark the $\delta = 0$ level. Note the larger scale bar range in (b).

dotted lines in Figure 10, the incoming critical pressure is equally described by both the B and T states.

Finally, we examine the cooperativity of the chemical and physical gradients in producing the critical pressure asymmetry. We do this by comparing the optimal critical pressure asymmetry to "the sum of its parts": the cooperativity δ is defined as

$$\delta = A - (A_{het}^{cyl} + A_{hom}^{con}) \tag{17}$$

At each (R_2', α) coordinate, A_{het}^{cyl} is evaluated as the critical pressure asymmetry of a cylindrical pore, with a chemical gradient the same as the optimal chemical gradient shown in Figure 10b,c. For a fair comparison, we also ensure the pore depth L is the same for the cylindrical and conical pores at each (R_2', α) coordinate. A_{hom}^{con} is the critical pressure asymmetry for a chemically homogeneous conical pore. A number of choices exist in deciding which homogeneous contact angle most fairly compares to the optimal chemical gradient. We show in Figure 11 the two limiting cases, when the homogeneous contact angle is (i) the optimal θ_1 at each (R_2', α) coordinate and (ii) the optimal θ_2 at each (R_2', α) coordinate. To distinguish these two limiting cooperativities, we label these δ_1 in Figure 11a and δ_2 in Figure 11b.

In Figure 11a, over the majority of the (R_2', α) plane, the cooperativity $\delta_1 > 0$, meaning that the optimal asymmetry (arising from both physical and chemical gradients) is greater than the sum of asymmetries arising from the physical gradient and chemical gradient separately. Thus, the physical and chemical gradients act together to produce the high optimal asymmetries. The exceptions to this, when $\delta_1 < 0$ within the solid black contours, arise when the optimal asymmetry is almost wholly achieved through the conical shape and not the chemical patterning. As $A_{het}^{cyl} > 0$, in these cases, the optimal asymmetry is less than the sum of its parts.

In Figure 11b, we observe an extended region at intermediate values of α for which the cooperativity $\delta_2 > 1$. This very large, positive cooperativity is caused in this region by the occurrence of the I-type outgoing critical meniscus for the homogeneous conical pore. The I-type outgoing critical pressure is smaller than the B or B′ types; hence, A_{hom}^{con} is small, leading to the large δ_2 observed. The impact of B- or B′-type outgoing critical pressures instead of I can be seen in Figure 11a. Here, the outgoing type is always B or B′, leading to a larger A_{hom}^{con} and hence a smaller δ_1.

IV. CONCLUSIONS

Here we have calculated the maximum Laplace pressures (the critical pressures) required for fluid to both enter and leave a conical, chemically patterned pore, sandwiched between two absorbent substrates. Across the range of pore designs considered, we found the Laplace pressure to depend on the contact line radius in four different manners, of which two of these arose from a competition between the physical and chemical gradients. This interaction between the two gradients produced three different critical menisci, where the contact line was pinned to the top of the pore, pinned to the bottom of the pore, or located in between. The presence of the top and bottom substrates produced an additional two critical menisci due to premature contact of the liquid–vapor interface with the substrates.

We then analyzed the critical pressure asymmetry, the difference between incoming and outgoing critical pressures, as a measure of the efficacy of the fluid diode across a range of pore geometries. For the pores considered with an opening angle $\alpha < 90°$, the outgoing pressure was always shown to be larger than the incoming pressure. Furthermore, the maximum asymmetry did not in general occur due to the dominance of either the incoming or outgoing critical pressure individually, but as a compromise between the two.

Finally, we optimized the chemical pattering to produce maximal critical pressure asymmetries across the range of pore geometries, showing that a large chemical gradient is required to produce large asymmetries. Across the majority of pore opening angles α and maximum radii R_2, we showed that the optimum asymmetry for the pore with both physical and chemical gradients was greater than the sum of asymmetries of pores with physical gradients and chemical gradients separately. The physical and chemical gradients therefore act together cooperatively to achieve the largest critical pressure asymmetries.

■ ASSOCIATED CONTENT

Supporting Information

The Supporting Information is available free of charge at https://pubs.acs.org/doi/10.1021/acs.langmuir.0c01039.

Derivation of the critical pressure asymmetry limits and proof that for $\alpha < \pi/2$ the asymmetry $A > 0$ (PDF)

https://dx.doi.org/10.1021/acs.langmuir.0c01039
Langmuir 2020, 36, 7463−7473

AUTHOR INFORMATION

Corresponding Author

Halim Kusumaatmaja − *Department of Physics, Durham University, Durham DH1 3LE, U.K.;* orcid.org/0000-0002-3392-9479; Email: halim.kusumaatmaja@durham.ac.uk

Authors

Jack R. Panter − *Department of Physics, Durham University, Durham DH1 3LE, U.K.;* orcid.org/0000-0001-8523-7629

Yonas Gizaw − *The Procter and Gamble Co., Mason, Ohio 45040, United States*

Complete contact information is available at: https://pubs.acs.org/10.1021/acs.langmuir.0c01039

Notes

The authors declare no competing financial interest.

ACKNOWLEDGMENTS

The authors thank Procter & Gamble for funding.

REFERENCES

(1) Li, J.; Li, J.; Sun, J.; Feng, S.; Wang, Z. Biological and Engineered Topological Droplet Rectifiers. *Adv. Mater.* **2019**, *31*, 1806501.

(2) Ju, J.; Bai, H.; Zheng, Y.; Zhao, T.; Fang, R.; Jiang, L. A multi-structural and multi-functional integrated fog collection system in cactus. *Nat. Commun.* **2012**, *3*, 1247.

(3) Bai, H.; Tian, X.; Zheng, Y.; Ju, J.; Zhao, Y.; Jiang, L. Direction Controlled Driving of Tiny Water Drops on Bioinspired Artificial Spider Silks. *Adv. Mater.* **2010**, *22*, 5521−5525.

(4) Kusumaatmaja, H.; Yeomans, J. M. Anisotropic hysteresis on ratcheted superhydrophobic surfaces. *Soft Matter* **2009**, *5*, 2704.

(5) Renvoisé, P.; Bush, J. W. M.; Prakash, M.; Quéré, D. Drop propulsion in tapered tubes. *Europhys. Lett.* **2009**, *86*, 64003.

(6) Lorenceau, L.; Quéré, D. Drops on a conical wire. *J. Fluid Mech.* **1999**, *510*, 29−45.

(7) Brochard, F. Motions of droplets on solid surfaces induced by chemical or thermal gradients. *Langmuir* **1989**, *5*, 432−438.

(8) de Gennes, P.-G.; Brochard-Wyart, F.; Quéré, D. *Capillarity and Wetting Phenomena: Drops, Bubbles, Pearls, Waves*; Springer Science + Business Media, Inc.: New York, 2010.

(9) Mates, J. E.; Schutzius, T. M.; Qin, J.; Waldroup, D. E.; Megaridis, C. M. The fluid diode: Tunable unidirectional flow through porous substrates. *ACS Appl. Mater. Interfaces* **2014**, *6*, 12837−12843.

(10) Zhang, S.; Huang, J.; Chen, Z.; Yang, S.; Lai, Y. Liquid mobility on superwettable surfaces for applications in energy and the environment. *J. Mater. Chem. A* **2019**, *7*, 38−63.

(11) Zhao, Y.; Wang, H.; Zhou, H.; Lin, T. Directional Fluid Transport in Thin Porous Materials and its Functional Applications. *Small* **2017**, *13*, 1601070.

(12) Brown, P. S.; Bhushan, B. Bioinspired materials for water supply and management: water collection, water purification and separation of water from oil. *Philos. Trans. R. Soc., A* **2016**, *374*, 20160135.

(13) Li, J.; Zhou, X.; Li, J.; Che, L.; Yao, J.; McHale, G.; Chaudhury, M. K.; Wang, Z. Topological liquid diode. *Sci. Adv.* **2017**, *3*, eaao3530.

(14) Shou, D.; Fan, J. An All Hydrophilic Fluid Diode for Unidirectional Flow in Porous Systems. *Adv. Funct. Mater.* **2018**, *28*, 1800269.

(15) Zimmermann, M.; Hunziker, P.; Delamarche, E. Valves for autonomous capillary systems. *Microfluid. Nanofluid.* **2008**, *5*, 395−402.

(16) Diersch, H.-J. G.; Clausnitzer, V.; Myrnyy, V.; Rosati, R.; Schmidt, M.; Beruda, H.; Ehrnsperger, B. J.; Virgilio, R. Modeling Unsaturated Flow in Absorbent Swelling Porous Media: Part 1. Theory. *Transp. Porous Media* **2010**, *83*, 437−464.

(17) Miao, D.; Huang, Z.; Wang, X.; Yu, J.; Ding, B. Continuous, Spontaneous, and Directional Water Transport in the Trilayered Fibrous Membranes for Functional Moisture Wicking Textiles. *Small* **2018**, *14*, 1801527.

(18) Shi, L.; Liu, X.; Wang, W.; Jiang, L.; Wang, S. A Self-Pumping Dressing for Draining Excessive Biofluid around Wounds. *Adv. Mater.* **2018**, *31*, 1804187.

(19) Cho, H.; Kim, H.-Y.; Kang, J. Y.; Kim, T. S. How the capillary burst microvalve works. *J. Colloid Interface Sci.* **2007**, *306*, 379−385.

(20) Chen, J. M.; Chen, C.-Y.; Liu, C.-H. Pressure Barrier in an Axisymmetric Capillary Microchannel with Sudden Expansion. *Jpn. J. Appl. Phys.* **2008**, *47*, 1683−1689.

(21) Taher, A.; Jones, B.; Fiorini, P.; Lagae, L. Analytical, numerical and experimental study on capillary flow in a microchannel traversing a backward facing step. *Int. J. Multiphase Flow* **2018**, *107*, 221−229.

(22) Kaufman, Y.; Chen, S.-Y.; Mishra, H.; Schrader, A. M.; Lee, D. W.; Das, S.; Donaldson, S. H.; Israelachvili, J. N. Simple-to-Apply Wetting Model to Predict Thermodynamically Stable and Metastable Contact Angles on Textured/Rough/Patterned Surfaces. *J. Phys. Chem. C* **2017**, *121*, 5642−5656.

(23) Panter, J. R.; Gizaw, Y.; Kusumaatmaja, H. Multifaceted design optimization for superomniphobic surfaces. *Sci. Adv.* **2019**, *5*, eaav7328.

(24) Ma, B.; Shan, L.; Dogruoz, B.; Agonafer, D. Evolution of Microdroplet Morphology Confined on Asymmetric Micropillar Structures. *Langmuir* **2019**, *35*, 12264−12275.

(25) Agonafer, D. D.; Lee, H.; Vasquez, P. A.; Won, Y.; Jung, K. W.; Lingamneni, S.; Ma, B.; Shan, L.; Shuai, S.; Du, Z.; Maitra, T.; Palko, J. W.; Goodson, K. E. Porous micropillar structures for retaining low surface tension liquids. *J. Colloid Interface Sci.* **2018**, *514*, 316−327.

(26) de Gennes, P.-G.; Brochard-Wyart, F.; Quéré, D. *Capillarity and Wetting Phenomena*; Springer: New York, 2004.

(27) Moebius, F.; Or, D. Interfacial jumps and pressure bursts during fluid displacement in interacting irregular capillaries. *J. Colloid Interface Sci.* **2012**, *377*, 406−415.

(28) Rabbani, H. S.; Seers, T. D. Inertia Controlled Capillary Pressure at the Juncture between Converging and Uniform Channels. *Sci. Rep.* **2019**, *9*, 13870.

(29) Gibbs, J. W. *The Scientific Papers of J. Willard Gibbs*; Longmans, Green and Co.: London, 1906; Vol. *1*.

(30) Blow, M. L.; Kusumaatmaja, H.; Yeomans, J. M. Imbibition through an array of triangular posts. *J. Phys.: Condens. Matter* **2009**, *21*, 464125.

(31) Lee, S.; Park, J.-S.; Lee, T. R. The Wettability of Fluoropolymer Surfaces: Influence of Surface Dipoles. *Langmuir* **2008**, *24*, 4817−4826.